ELSEVIER

Journal of Fluids and Structures 24 (2008) 559–575

JOURNAL OF
FLUIDS AND
STRUCTURES

www.elsevier.com/locate/jfs

An improved three-dimensional coupled fluid–structure model for Coriolis flowmeters

N. Mole[a,*], G. Bobovnik[b], J. Kutin[b], B. Štok[a], I. Bajsić[b]

[a]Laboratory for Numerical Modelling and Simulation, Faculty of Mechanical Engineering, University of Ljubljana, Aškerčeva 6, SI-1000 Ljubljana, Slovenia
[b]Laboratory of Measurements in Process Engineering, Faculty of Mechanical Engineering, University of Ljubljana, Aškerčeva 6, SI-1000 Ljubljana, Slovenia

Received 18 April 2007; accepted 8 October 2007
Available online 4 March 2008

Abstract

The paper presents a coupled numerical model built to simulate the operation of Coriolis flowmeters, which exploit the alteration of the vibration mode shape of the measuring tube for the mass flow rate measurement. The explained measuring effect is a consequence of the interaction between the motion of the tube, vibrating at its natural frequency, and the fluid flow in it. The numerical model is realized by coupling of a finite volume (FV) code for fluid flow analysis with a finite element (FE) code for structural analysis using the conventional staggered solution procedure, with added inner iterations to achieve strong coupling. The simulation algorithm is divided into two steps. A free vibration of the measuring tube considered in the first step is complemented in the second step, after the numerical free vibration response is properly stabilized, with the harmonic excitation force actuating the measuring tube at its resonant frequency of several hundreds of Hertz to resemble the operation of actual Coriolis flowmeters. Different scenarios using zero-order or three-point fluid load predictor and soft application of the fluid load in the initial stages of the simulation are compared to yield a simulation strategy, which will minimize the time needed to obtain the stabilized steady-state response of the vibrating measuring tube. The proposed simulation procedure was applied on a straight-tube Coriolis flowmeter and used for the estimation of the velocity profile effect. The results exhibit sufficient stability (low scatter) to be used for the estimation of sensitivity variations of order of magnitude around tenths of a percent.

Keywords: Coriolis flowmeter; Fluid–structure interaction; Coupled numerical model; Velocity profile effect

---

1. Introduction

The primary sensing element in the Coriolis mass flowmeter is a fluid-conveying measuring tube that is maintained vibrating periodically at its natural frequency under imposed forced vibration conditions (resonance). The result of interaction between the motion of the tube and the fluid flow is exhibited as the distortion of symmetry of the no-flow drive mode, which is mainly a consequence of the Coriolis inertial force field. Such alteration, manifested in an antisymmetric way for a straight measuring tube clamped at both ends and vibrating at its first natural frequency, is

---

*Corresponding author. Tel.: +386 1 4771 425; fax: +386 1 2518 567.
E-mail address: nikolaj.mole@fs.uni-lj.si (N. Mole).

doi:10.1016/j.jfluidstructs.2007.10.004

schematically shown in Fig. 1. Mass flow is usually measured as the time or phase difference between the motion of two sensing points on the tube, which are positioned symmetrically along the tube length (such as S_1 and S_2 in Fig. 2).

Coriolis flowmeters are employed for mass flowrate measurements in different applications: from water-like fluids to heavy viscous oils, gases, two-component flows, etc. (Baker, 2000). Since the new generation of Coriolis flowmeters try to achieve accuracies smaller than 0.1% for mass flow rate measurements, knowledge and thorough understanding of all potential influences contributing to the Coriolis measuring effect is required. One of the only partially explored effects is surely the velocity profile effect (Kutin et al., 2006). The modelling concepts, which have so far been applied for predictions of three-dimensional flow effects in Coriolis flowmeters, can be classified into analytical and numerical models. The analytical approach, which is no doubt extremely helpful for getting a sound physical insight, proves however to be efficient only in simple configurations, while the numerical models take advantage of being more convenient, even if not really efficient, for more general configurations and applications of flowmeters. The modelling of Coriolis flowmeters can be usefully based on the scientific foundation of fluid–structure interactions. Considering their construction characteristics, Coriolis flowmeters represent an engineering example of slender system interacting with axial flow (Païdoussis, 1998, 2004).

This paper presents further development of a three-dimensional coupled fluid–structure numerical model of the Coriolis flowmeter first presented in Bobovnik et al. (2005). The numerical model is based on a partitioned numerical approach (Piperno, 1997; Piperno et al., 1997; Farhat and Lesoinne, 2000; Piperno and Farhat, 2001; Felippa et al., 2001), where the structure and the fluid equations are solved in an alternate fashion, with the interface conditions enforced asynchronously. We employed a finite volume (FV) code for the analysis of viscous turbulent three-dimensional fluid flow and a finite element (FE) code for the analysis of deformable vibrating measuring tube. Implicit coupling of the two solvers or a strong coupling procedure was achieved by adding the inner iterations within each time step of the simulation, and the block-Gauss–Seidel method (often called a "staggered solution procedure") was applied for the solution of the global system of nonlinear equations (Matthies and Steindorf, 2003; Matthies et al., 2006). The procedure starts with solving one of the systems, where the interface conditions, defined with the other subsystem, have

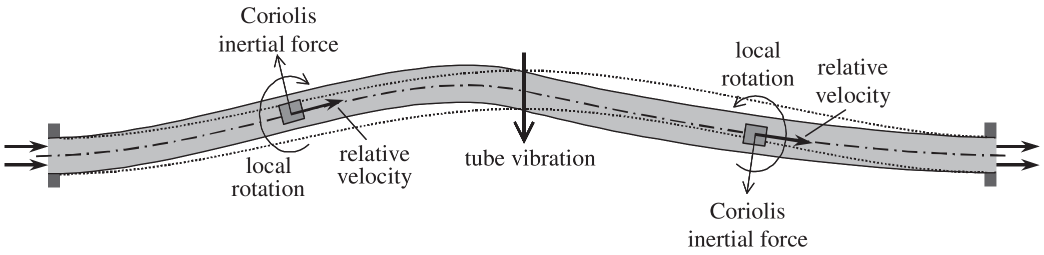

Fig. 1. Schematic representation of the Coriolis measuring effect.

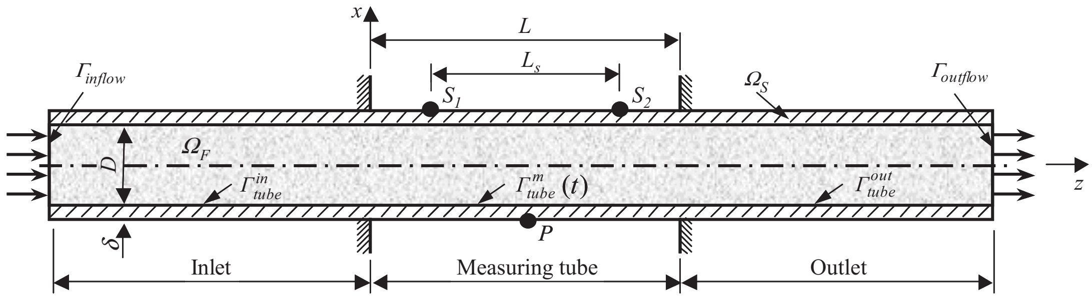

$$\Gamma^{in}_{tube} \cup \Gamma^{m}_{tube}(t) \cup \Gamma^{out}_{tube} = \Gamma_{tube}(t)$$

$$\Gamma^{u}_{tube} \cup \Gamma^{\sigma}_{tube}(t) = \Gamma^{m}_{tube}(t)$$

Fig. 2. Model of the Coriolis flowmeter.

to be predicted. In contrast to the majority of procedures, which use a prediction of structural displacement in the subsequent time step, the present analysis employs a fluid load predictor. The latter proved to be more favourable regarding the computational time (or inner iterations per time step) needed for the cases analysed. Besides the fluid load zero-order predictor (already used by Engel and Griebel, 2006), a three-point prediction of the fluid load was also introduced.

The improvements of the three-dimensional coupled fluid–structure numerical model of the Coriolis flowmeter, which are introduced in this paper, have the following objectives: (i) to achieve better resemblance between the numerical model response and the true operation of the Coriolis flowmeter, (ii) to minimize the scatter due numerical noise of the calculated responses (e.g. phase differences) in the steady-state (periodic) conditions, and (iii) to minimize the computational time needed to obtain a steady-state response of the flowmeter.

Thus, being aware of the fact that the vibration of the measuring tube in actual Coriolis flowmeters is maintained by the action of the excitation force, the numerical model has been complemented to address properly the forced vibration conditions. The simulation procedure has been separated into two successive steps, *Step I* and *Step II*, addressing, respectively, the free-vibration response and the forced-vibration response of the considered coupled system. In this paper, Step I, which relies essentially on the simulation strategy used in Bobovnik et al. (2005), is used only to obtain the input data for the transition to Step II of the simulation. The measuring effect (the time or phase difference) of the Coriolis flowmeter is calculated from several cycles of the steady-state response. Section 3 describes the strategies used for obtaining the optimal computational efficiency and accuracy of the numerical model, such as soft application of the fluid forces in the starting stages of Step I, a procedure for smooth transition from Step I to II and prediction of the fluid forces to be considered in the next time step.

The new three-dimensional coupled numerical model is employed for a clamped, straight-tube configuration of the Coriolis flowmeter under different inflow conditions of a water-like fluid, which discussed in Section 4. The actions taken to improve the stability of calculated responses and to minimize the computational time are analysed in Sections 4.1 and 4.2 for Steps I and II, respectively. Finally, in Section 4.3 the results of the velocity profile effect obtained with the coupled numerical model are presented. The calculated sensitivity decrease for lower Reynolds numbers is compared with the analytical results of the weight vector theory.

2. Mathematical model

2.1. Model definition

The model of the Coriolis flowmeter considered in this paper is schematically presented in Fig. 2. It consists of a straight measuring tube that is clamped at both ends and vibrates in the first bending mode under imposed forced vibration conditions in the x–z plane. The external excitation force is applied at point P in the central cross-section of the measuring tube (Fig. 2). Because deformation of the measuring tube is small enough, linear elastic theory is used. The effect of the sensors and possible added masses of the excitation system on the motion of the measuring tube is neglected in the model under consideration. A fully developed flow, with a prescribed inlet flow profile, of Newtonian, turbulent, isothermal and weakly compressible fluid is considered in the measuring tube.

In general, let us denote by $\Omega_F(t)$ the domain of interest, assumed to be filled by a fluid, and its boundary by $\Gamma_F(t)$, both subject to variation with time. For the problem considered the domain $\Omega_F(t)$ is actually represented by the flowing fluid within the pipe-segment under consideration, and accordingly the boundary $\Gamma_F(t)$ can be decomposed into three parts Γ_{inflow}, Γ_{outflow} and $\Gamma_{\text{tube}}(t)$, denoting in turn the inlet and outlet cross-sections, and the part in contact with the fluid-conveying tube (Fig. 2). The latter can be further decomposed into $\Gamma^{\text{in}}_{\text{tube}}$ and $\Gamma^{\text{out}}_{\text{tube}}$, corresponding to the fixed inlet and outlet part of the tube, and the remaining oscillating part of the tube in between $\Gamma^{m}_{\text{tube}}(t)$ (Fig. 2).

Again, let us denote, in general, by $\Omega_S(t)$ the domain of interest, assumed to be occupied by a solid, and its boundary by $\Gamma_S(t)$, both of which can vary with time. To be compatible with the given fluid domain definition for the Coriolis flowmeter problem the domain $\Omega_S(t)$ is represented by the pipe-segment containing the considered fluid domain $\Omega_F(t)$. The corresponding boundary $\Gamma_S(t)$, which consists of the external and internal surface of the fluid-conveying tube, can be decomposed into three parts: the inlet and outlet fixed part of the tube, and the oscillating part of the tube in between, which is actually used for measurement. When referring to the internal surface of the measuring part of the tube, which is in contact with the fluid, we will use the notation Γ^{u}_{tube} for the fixed boundary, and $\Gamma^{\sigma}_{\text{tube}}(t)$ for the boundary, where the surface distributed load is applied (Fig. 2).

2.2. Fluid dynamics problem

2.2.1. Governing equations

The three-dimensional spatial distribution ($\mathbf{x} \in \Omega_F$) and time evolution ($t > 0$) of fluid flow are governed by the conservation of mass and momentum principles, mathematically written in the integral form as

$$\frac{\partial}{\partial t}\int_{\Omega_F} \rho_F \, \mathrm{d}\Omega + \int_{\Gamma_F} \rho_F (\mathbf{v}_F - \mathbf{v}_S) \cdot \mathbf{n} \, \mathrm{d}\Gamma = 0, \tag{1}$$

$$\frac{\partial}{\partial t}\int_{\Omega_F} \rho_F \mathbf{v}_F \, \mathrm{d}\Omega + \int_{\Gamma_F} \rho_F \mathbf{v}_F (\mathbf{v}_F - \mathbf{v}_S) \cdot \mathbf{n} \, \mathrm{d}\Gamma = \int_{\Gamma_F} \boldsymbol{\sigma}_F \cdot \mathbf{n} \, \mathrm{d}\Gamma + \int_{\Omega_F} \mathbf{f}_F \, \mathrm{d}\Omega. \tag{2}$$

Movement of fluid particles, with the density $\rho_F(\mathbf{x},t)$ and the velocity field $\mathbf{v}_F(\mathbf{x},t)$ in the domain Ω_F ($\mathbf{x} \in \Omega_F$), is influenced by the motion of a surrounding boundary prescribed by the boundary velocity v_S of the volume Ω_F. The vector $\mathbf{f}_F(\mathbf{x},t)$ in the momentum equation (2) stands for the volume forces acting inside the domain Ω_F, and $\boldsymbol{\sigma}_F(\mathbf{x},t)$ is the resulting stress tensor, which is composed of the fluid stress tensor $\boldsymbol{\sigma}_f(\mathbf{x},t)$ and Reynolds stress tensor $\boldsymbol{\sigma}_t(\mathbf{x},t)$. The fluid stress tensor $\boldsymbol{\sigma}_f(\mathbf{x},t)$ is defined as

$$\boldsymbol{\sigma}_f = \mu(\operatorname{grad} \mathbf{v}_F + (\operatorname{grad} \mathbf{v}_F)^{\mathrm{T}}) - \tfrac{2}{3}\mu \operatorname{div} \mathbf{v}_F \mathbf{I} - p\mathbf{I}, \tag{3}$$

with p being the fluid pressure, $\mathbf{I}$ the unit tensor and μ the dynamic viscosity, while Reynolds stress tensor $\boldsymbol{\sigma}_t(\mathbf{x},t)$ (for Reynolds numbers, $\mathrm{Re} = v_F \, D \, \rho_F/\mu$, greater than 2300), which results from the fluid turbulence, is given according to the assumed k–ε turbulence model by

$$\boldsymbol{\sigma}_t = \mu_t(\operatorname{grad} \mathbf{v}_F + (\operatorname{grad} \mathbf{v}_F)^{\mathrm{T}}) - \tfrac{2}{3}(\mu_t \operatorname{div} \mathbf{v}_F + \rho_F k)\mathbf{I}, \tag{4}$$

where the turbulent viscosity μ_t depends on the turbulent kinetic energy k and its dissipation rate ε [see Pope (2000) for further details].

Considering the finite-volume discretization of the fluid domain, which involves FVs with moving boundaries (moving grid simulation), the so-called geometric conservation law (Thomas and Lombard, 1979),

$$\frac{\partial}{\partial t}\int_{\Omega_{FV}} \mathrm{d}\Omega + \int_{\Gamma_{FV}} \mathbf{v}_{FV}.\mathbf{n}_{FV} \, \mathrm{d}\Gamma = 0, \tag{5}$$

which links the rate of change of FV Ω_{FV} and FV boundary velocity $\mathbf{v}_{FV}$, has to be satisfied in addition to the above equations in order to assure that the mesh movement does not have any influence on the flow field.

2.2.2. Initial and boundary conditions

The initial velocity field $\mathbf{v}_F(\mathbf{x},0)$ and the stress field $\sigma_F(\mathbf{x},0)$ in the fluid may be assumed identical to the steady-state fields corresponding to the fully developed velocity profiles reached in a tube at rest. This can be obtained upon preliminary simulation of the fluid flow in a sufficiently long tube under considered inflow conditions and prescribed ambient pressure at the outflow boundary. The same fully developed velocity profile can be set as the prescribed boundary condition at the inflow boundary, while at the outflow boundary the ambient pressure is imposed.

Considering the described decomposition of the boundary $\Gamma_F(t)$ and physical nature of the associated boundary conditions, the respective boundary conditions for the assumed viscous flow can be written as

$$\begin{aligned}
&\mathbf{v}_F(\mathbf{x}, t) = \mathbf{v}_{\text{inflow}}, \quad \mathbf{x} \in \Gamma_{\text{inflow}},\\
&p(\mathbf{x}, t) = p_{\text{outflow}}, \quad \mathbf{x} \in \Gamma_{\text{outflow}},\\
&\mathbf{v}_F(\mathbf{x}, t) = \mathbf{v}_S(\mathbf{x}, t), \quad \mathbf{x} \in \Gamma^{m}_{\text{tube}}(t),\\
&\mathbf{v}_F(\mathbf{x}, t) = \mathbf{0}, \quad \mathbf{x} \in \Gamma^{\text{in}}_{\text{tube}} \vee \mathbf{x} \in \Gamma^{\text{out}}_{\text{tube}}.
\end{aligned} \tag{6}$$

The prescribed quantities in Eq. (6) are as follows: $\mathbf{v}_{\text{inflow}}$ is the inflow fluid velocity, p_{outflow} is the absolute fluid pressure at fluid outflow, and $\mathbf{v}_S(\mathbf{x},t)$ is the velocity of the measuring tube surface.

2.3. Structural dynamics problem

2.3.1. Governing equations

The three-dimensional spatial distribution ($\mathbf{x} \in \Omega_S$) and time evolution ($t > 0$) of the structural response is governed by the conservation of momentum principles. The respective equation of motion can be derived by Hamilton's variational principle, which may be written as

$$\int_{t_1}^{t_2} \delta(W_p - W_k)\,\mathrm{d}t = 0, \tag{7}$$

where W_p and W_k are, respectively, the total potential energy and the total kinetic energy of the moving solid structure considered.

The total potential energy W_p is composed as a sum of the strain energy corresponding to the actual deformation of the shell, and the load potential corresponding to the actually applied conservative external forces. Considering the nature of the investigated case, the surface tractions $\mathbf{p}_S(\mathbf{x},t)$ acting upon the moving shell boundary through the respective displacement field $\mathbf{u}_S(\mathbf{x},t)$, and the concentrated force $\mathbf{F}(t)$ at point P (Fig. 2), where the forced vibration is generated, are taken into account. Those loads yield the following integral expression for the total potential energy:

$$W_p = \frac{1}{2}\int_{\Omega_S} \boldsymbol{\sigma}_S : \boldsymbol{\varepsilon}_S\,\mathrm{d}\Omega - \int_{\Gamma_S} \mathbf{p}_S.\mathbf{u}_S\,\mathrm{d}\Gamma - \mathbf{F}.\mathbf{r}_P. \tag{8}$$

In the above equation $\boldsymbol{\varepsilon}_S(\mathbf{x},t)$ and $\boldsymbol{\sigma}_S(\mathbf{x},t)$ are, respectively, the strain and the stress tensor in the shell structure, and $\mathbf{r}_P$ is the position vector of point P where the force $\mathbf{F}$ is applied. The total kinetic energy W_k of the structure can be written as

$$W_k = \frac{1}{2}\int_{\Omega_S} \rho_S(\mathbf{v}_S \cdot \mathbf{v}_S)\,\mathrm{d}\Omega, \tag{9}$$

where $\rho_S\ (\mathbf{x},t)$ is the structure material density and $\mathbf{v}_S\ (\mathbf{x},t)$ is the structure velocity field.

2.3.2. Initial and boundary conditions

Being interested in the determination of the structural dynamic response of the tube under forced vibration conditions and some prescribed inlet flow conditions, the initial configuration $\Omega_S(0)$ may be set accordingly to the approach used in the fluid flow analysis. For a complete mechanical response definition of the straight tube at time $t = 0$, however, the initial velocity and acceleration fields, $\mathbf{v}_S(\mathbf{x},0)$ and $\mathbf{a}_S(\mathbf{x},0)$, respectively, must be given. The corresponding initial mechanical state is assumed unstressed and unstrained, therefore $\boldsymbol{\sigma}_S(\mathbf{x},0) = \boldsymbol{\varepsilon}_S(\mathbf{x},0) = \mathbf{0}$. At time $t > 0$ the problem is determined by the respective boundary conditions which, in view of the above-assumed external actions, take the following form:

$$\begin{aligned}
&\mathbf{u}_S(\mathbf{x},t) = \mathbf{0}, \quad \mathbf{x} \in \Gamma^u_{\text{tube}},\\
&\boldsymbol{\sigma}_S(\mathbf{x},t)\cdot\mathbf{n}(\mathbf{x},t) = \mathbf{p}_S(\mathbf{x},t), \quad \mathbf{x} \in \Gamma^\sigma_{\text{tube}}(t),\\
&\mathbf{F}(t) = (F(t),0,0), \quad \mathbf{x} = \mathbf{x}_P.
\end{aligned} \tag{10}$$

The time evolution of the structural mechanical response at time $t > 0$ is then governed, considering the just stated initial conditions and imposed boundary conditions, by the domain equations (7)–(9). It is, however, obvious that in the structural dynamics analysis only the measuring tube, clamped at both ends, will be taken into account.

2.4. Coupled fluid–structure dynamics problem

Each of the individual functional relationships, given in a single domain representation by Eqs. (1)–(6) and (7)–(10) for the fluid and structural dynamics problem, respectively, expresses a unique condition for determination of the respective field responses. Unfortunately, in the coupled fluid–structure problem a precise quantitative definition of that part of boundary conditions, which is related in (6) and (10) to the interaction effects that are transmitted through the common fluid–structure interface, is not available. Instead, interface conditions respecting physical consistency of the corresponding primary and secondary field variables have to be established iteratively during the computation, and fulfilled finally by the two subsystem solutions. In this context the governing domain equations, as given by (1), (2), (5) and (7) for the single domain uncoupled problems, are to be respected in the coupled problem as well. The major trouble associated with the finding of a given coupled problem solution, when the partitioned analysis approach is adopted, thus lies in the mutual fulfillment of the consistency conditions of the two field responses at the common interface $\Gamma_{FS}(t)$ (Fig. 3). Since none of the problem variables are given explicitly there, the stress–displacement compatibility between the field variables of the respective subsystems in contact is established implicitly by imposing kinematic and contact stress constraints. With $\mathbf{n}(\mathbf{x},t)$ denoting the normal vector at the interface $\Gamma_{FS}(t)$ these constraints are formulated as follows:

$$\boldsymbol{\sigma}_F(\mathbf{x},t)\cdot\mathbf{n}(\mathbf{x},t) = \boldsymbol{\sigma}_S(\mathbf{x},t)\cdot\mathbf{n}(\mathbf{x},t), \quad \mathbf{u}_F(\mathbf{x},t) = \mathbf{u}_S(\mathbf{x},t), \ \ \mathbf{x} \in \Gamma_{FS}(t). \tag{11}$$

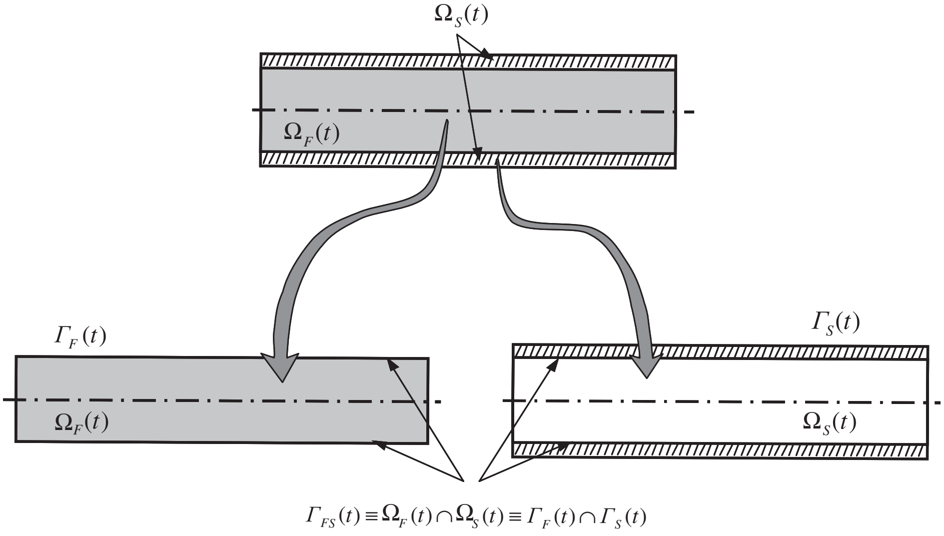

Fig. 3. Fluid–structure domain decomposition and interface definition.

3. Coupled fluid–structure simulation strategy

In general, considering its dependence both on characteristics of the flowmeter and the fluid, the undamped natural frequency ω_0 of the coupled system is not known in advance. The true operating conditions of the flowmeter in an experimental environment are found by a procedure in which the applied excitation frequency is adequately adjusted to become finally equal to the frequency ω_0. We are confronted with quite the same task when considering the problem computationally. To achieve a fast numerical periodic steady-state response of the considered coupled system, which should be excited at a particular undamped natural frequency of the coupled system, a special two-step solution procedure has been developed. The main idea behind this procedure is to ensure monotonic and smooth convergence by finding first the stabilized periodic response of the free oscillating coupled system, and only then, with the natural frequency of the coupled system having been determined, to proceed with the simulation of the excited tube vibration. Simply said, we find the undamped natural frequency ω_0 of the system first, and then, considering that the oscillation is damped, we apply the excitation force to keep the system in oscillation. The two basic steps of our solution procedure cover actually these actions (Fig. 4).

In order to provide data for the numerical simulation of the considered fluid–structure problem, some preliminary computations are needed first. The initial fluid kinematic conditions and loads are thus obtained from the steady-state fluid flow analysis in the tube at rest, whereas the initial velocity field of the tube is determined corresponding to the first natural vibration mode. The equivalent stiffness of the measuring tube that is needed in Step II can be determined at this stage as well. With the initial conditions determined, we can proceed to Step I in which a stabilized periodic response of the system in free vibration motion is looked for. The oscillation being affected both by physical and numerical damping, the characterization of the response includes determination of the first damped frequency ω_D and actual damping factor ζ. Considering the equivalent stiffness of the measuring tube and having obtained in Step I the properties of the free oscillating system, proper parameters of the forcing function are then established; its action is followed in Step II, where a periodic steady-state response of the system under imposed excitation is looked for.

The two steps, i.e. Steps I and II, are addressed in Sections 3.2 and 3.3, respectively, while the numerical model used for computer simulation of the considered coupled fluid–structure problem is described in detail in Section 3.1.

3.1. Numerical model and solution procedure

The numerical model used for computer simulation is a partitioned one. It is built by linking the FV commercial code Star-CD v3.26 for the analysis of viscous and turbulent three-dimensional fluid flow with the FE commercial code Abaqus 6.5 for the analysis of a vibrating measuring tube, which is analysed as a deformable shell structure.

The Star-CD code uses the FVM to transform the governing differential equations into finite-difference equations. The unsteady terms are discretized in accordance with the first-order implicit Euler scheme. The convective terms in the

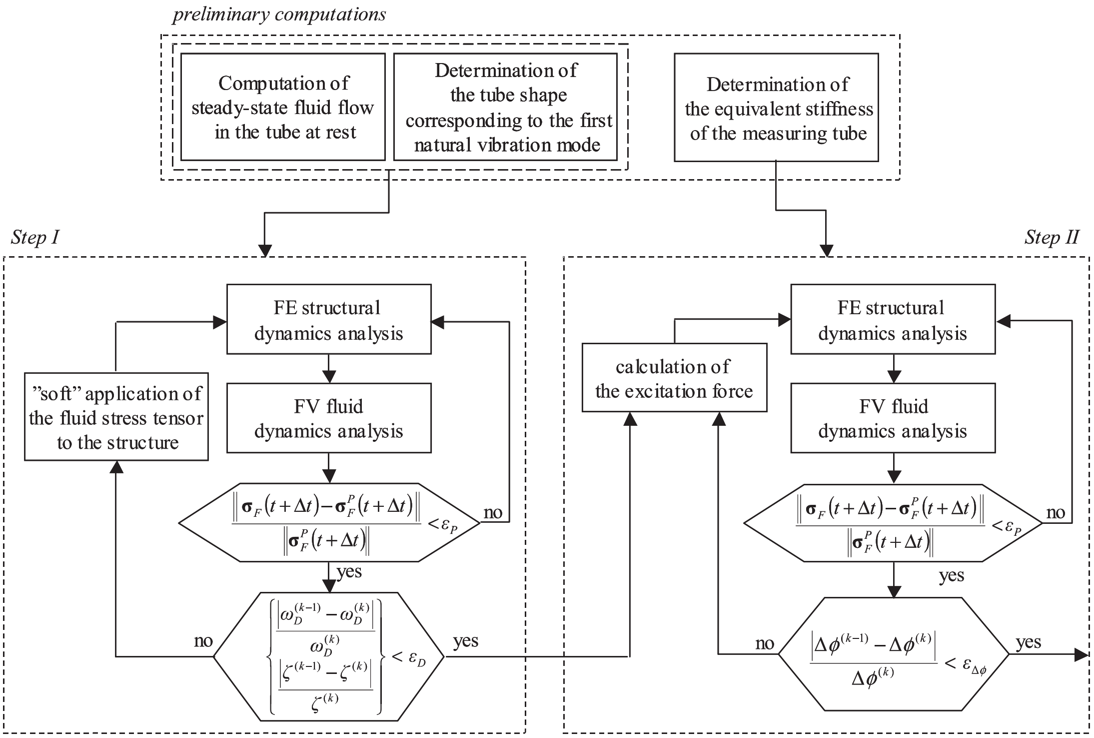

Fig. 4. Block diagram of the simulation strategy.

governing fluid equations are approximated using the second-order central difference scheme and the diffusive terms by the face-centred expression.

The Abaqus code solves a dynamics problem in accordance with the FEM. The dynamics equilibrium equations are solved and the values of the unknowns are determined at the end of a time step, based on the knowledge of their values at the beginning of the considered time step. The Newmark formulae are used for implicit displacement and velocity time integration.

From the computational point of view, we are basically confronted with two tasks. The first regards time integration, which is performed stepwise, while the second deals with strategies to be used for efficient coupling of the individual domain solutions and their convergence in time. In accordance with the adopted partitioned analysis approach the conventional serial staggered procedure (Felippa et al., 2001) is used. Physical consistency of the problem quantities at the fluid–structure interface at each time step is achieved iteratively. To avoid extrapolation of the quantities transmitted across the fluid–structure interface, it is required that the respective fluid FV and structural FE subdomain discretizations match at the fluid–structure interface. The node coincidence of the two meshes at the fluid–structure interface is assured by dragging the respective nodes of the FV mesh as if they were attached to the tube, i.e. by following directly the motion of the respective nodes of the FE mesh as it is obtained by a corresponding analysis of the structural problem within a given time interval. At the same time, the internal nodes of the FV mesh have to be adequately adjusted in order to preserve the same FV discretization topology in time.

The solution procedure will thus be characterized by alternative exchange of the data between the two computational codes, where the data generated within one code upon given initial and boundary conditions will provide information to be used in the subsequent numerical step as updated initial and boundary conditions for the other code.

Assuming that at a certain time t the dynamic equilibrium in the coupled system is attained within a given tolerance, the time can be advanced $t \to t+\Delta t$ and the procedure to find the respective equilibrium can begin. Our staggered solution procedure, which is shown schematically in Fig. 5, can be formulated by the following sequence of steps.

Step 1: The initial guess for the fluid load in the new time step $t+\Delta t$ is based upon the known values of the fluid stress tensor from the preceding time steps. In our investigation it is approximated either by a zero-order predictor

$$\boldsymbol{\sigma}_F^P(t+\Delta t) = \boldsymbol{\sigma}_F(t) \tag{12}$$

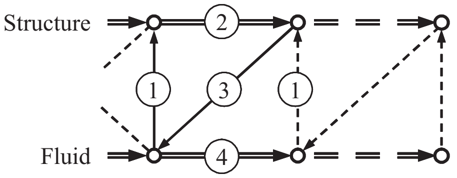

Fig. 5. Staggered coupling procedure.

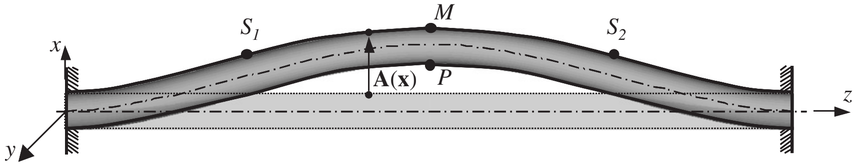

Fig. 6. The first mode shape of the measuring tube without fluid flow.

or by a three-point predictor based on known fluid stress data from the preceding three time steps. The latter can be written, when assuming a constant time step size, in the following form:

$$\boldsymbol{\sigma}_F^P(t+\Delta t) = 3(\boldsymbol{\sigma}_F(t) - \boldsymbol{\sigma}_F(t-\Delta t)) + \boldsymbol{\sigma}_F(t-2\Delta t). \tag{13}$$

Step 2: Considering the mechanical state obtained in the tube at the end of the preceding time step, the structural system is advanced to $t+\Delta t$ under load $\mathbf{p}_S(t+\Delta t)$ induced by the fluid,

$$\mathbf{p}_S(t+\Delta t) = -\boldsymbol{\sigma}_F^P(t+\Delta t).\mathbf{n}_S, \quad \mathbf{x} \in \Gamma_{FS}, \tag{14}$$

where the normal $\mathbf{n}_S$ refers to the structure.

Step 3: The motion of the wet boundary of the tube is transferred to the fluid

$$\mathbf{u}_F(t+\Delta t) = \mathbf{u}_S(t+\Delta t), \quad \mathbf{x} \in \Gamma_{FS}, \tag{15}$$

the position of the fluid mesh is updated and the grid velocities $\mathbf{v}_S$ calculated considering the geometric conservation law (5) in its discretized form corresponding to the selected time scheme (Ferziger and Perić, 1999).

Step 4: Considering the dynamic state obtained in the fluid at the end of the preceding time step the fluid system is advanced to $t+\Delta t$ and the new fluid stress tensor $\boldsymbol{\sigma}_F(t+\Delta t)$ is computed. The calculated fluid stress tensor is compared with its initial prediction

$$\frac{\|\boldsymbol{\sigma}_F(t+\Delta t) - \boldsymbol{\sigma}_F^P(t+\Delta t)\|}{\|\boldsymbol{\sigma}_F^P(t+\Delta t)\|} < \varepsilon_P. \tag{16}$$

If the norm is larger than the prescribed tolerance ε_P, return to Step 2, substituting the predicted fluid stress tensor $\boldsymbol{\sigma}_F^P$ with the calculated one $\boldsymbol{\sigma}_F$ and starting the inner iteration loop, i.e. repeating the solution procedure. If the norm is smaller than the prescribed tolerance, return to Step 1 and proceed to the next time step.

3.2. Step I—free vibration of the coupled system

The computational analysis of the fluid–structure system starts with the computation of the structural response of the undeformed tube upon prescribed initial kinematic conditions and fluid loads that have been obtained by the steady-state flow conditions in the tube at rest. Initial kinematic conditions are considered as follows:

$$\begin{aligned} &\mathbf{u}(\mathbf{x},0) = \mathbf{0}, \\ &\mathbf{v}(\mathbf{x},0) = \beta\mathbf{A}(\mathbf{x}), \quad \mathbf{x} \in \Omega_S, \\ &\mathbf{a}(\mathbf{x},0) = \mathbf{0}, \end{aligned} \tag{17}$$

with the amplitude vector field $\mathbf{A}(\mathbf{x})$ being determined independently in accordance with the first natural vibration mode of the tube (Fig. 6). The scalar β is a constant multiplier, its magnitude being adjusted to meet the maximum deflection requirement, which is set at a value of about one-tenth of the tube inner diameter.

According to the described staggered procedure, the induced vibration yields in the first time step of the coupled simulation the displacement and velocity vectors of the tube. With the new displaced tube geometry and computed velocity vectors imposed as the boundary conditions in the fluid flow simulation, the respective stress and velocity response of the fluid for the same time interval are obtained, as a response of the fluid to the induced vibration of the tube. In case the prescribed convergence criteria are not satisfied, a further inner iteration cycle is needed. The described coupling procedure works in principle, but because of the pronounced inertial effects of non-equilibrated forces in the initial stage of computation, it needs in its elementary form a rather long time to establish stabilized periodic response. Regarding this issue, a considerable improvement can be done, however. Our primary concern in the considered numerical analysis is actually to establish a stabilized periodic response of the coupled system, with the initial disturbance faded away. In this respect a departure from the physically exact fulfillment of the coupling conditions in the beginning of computation would be acceptable, if beneficial for the shortening of the overall computational time. In this sense we found it computationally efficient to use in the early stages of computation the so-called soft application of the fluid pressure to the structure. By including the load factor α $(0 \leqslant \alpha(t) \leqslant \alpha(t+\Delta t) \leqslant 1)$, Eq. (14) is appropriately modified and reads

$$\mathbf{p}_S(t+\Delta t) = -\alpha(t)\boldsymbol{\sigma}_F^P(t+\Delta t).\mathbf{n}_S, \quad \mathbf{x} \in \Gamma_{FS}. \tag{18}$$

The time variation of the load factor assumed in our investigation is shown in Fig. 7. Impact of three different combinations of n_1 and n_2 used are discussed in Section 4, where computer simulation results are presented.

When the total fluid pressure is applied to the structure, the evaluation of the first damped frequency ω_D and the damping factor ζ of the fluid-conveying measuring tube under free vibration can begin. The difference between the respective computed values in the last two oscillation cycles is monitored and compared to the prescribed value, according to the following relations:

$$\frac{|\omega_D^{(k-1)} - \omega_D^{(k)}|}{\omega_D^{(k)}} < \varepsilon_D \quad \text{and} \quad \frac{|\zeta^{(k-1)} - \zeta^{(k)}|}{\zeta^{(k)}} < \varepsilon_D, \tag{19}$$

where index k stays for the kth, i.e. the last considered oscillation cycle. Because of the initial transient behaviour, at least three consecutive oscillation cycles are needed to determine the quantities of interest within the prescribed tolerance.

3.3. Step II—forced vibration of the coupled system

To reach a periodic steady-state response of the system under forced vibration conditions as effectively as possible, it is of crucial importance to properly specify parameters of the excitation force $\mathbf{F}(t)$, which is applied to the system at point P (Fig. 6) in order to balance the damping effect. The excitation force is harmonic in time, thus

$$\mathbf{F}(t) = (F_0 \sin(\omega_F t + \phi_F), 0, 0) \tag{20}$$

with F_0, ω_F and ϕ_F representing the force amplitude, the frequency of forced vibration and the initial phase, respectively.

Because the flowmeter operates at resonance, the forcing frequency ω_F is set equal to the natural frequency of the coupled system, i.e. $\omega_F = \omega_0$. Using the parameters of the damped free oscillation from Step I, the undamped natural frequency ω_0 is calculated as

$$\omega_0 = \frac{\omega_D}{\sqrt{1-\zeta^2}}, \tag{21}$$

in analogy with a harmonically excited one-dof damped oscillator, shown in Fig. 8. The force amplitude F_0 should be chosen so that a periodic steady-state response of the excited system would be attained as quickly as possible. Balancing of the damping effect is most efficient when the imposed excitation preserves displacement amplitude u_0 of the free vibrating system, computed just before the excitation force is included in the simulation. Therefore, still using the one-dof damped oscillator analogy, the force amplitude F_0 is calculated according to

$$F_0 = 2\zeta K_{\text{tube}} u_0, \tag{22}$$

where K_{tube} is the equivalent stiffness of the measuring tube. Due to the relatively small deflection of the measuring tube, the stiffness K_{tube} is computed from the assumed linear relationship between a static force, applied to the measuring tube at point P, and the respective displacement of that point. To assure a smooth transition from the free to the forced vibration, the initial phase ϕ_F has to be selected adequately also.

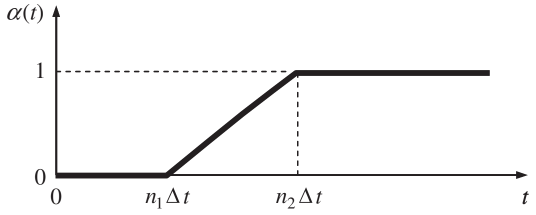

Fig. 7. Time variation of the load factor.

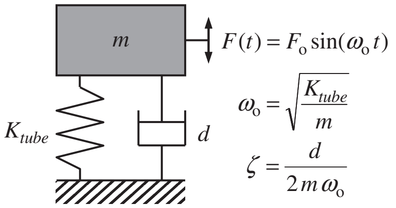

Fig. 8. One-dof damped oscillator.

4. Simulation results

The analysed Coriolis flowmeter, with geometry as presented in Fig. 2, is characterized by the length $L = 20D$ of a straight measuring part of the tube and a cross-section geometry which is determined by the internal diameter $D = 20\,\text{mm}$ and wall thickness $\delta = D/40$. The distance between the symmetrically positioned sensing points S_1 and S_2 is equal to $L_S = 10D$. The tube is supposed to be made of titanium with density $4510\,\text{kg/m}^3$, Young's modulus 102 700 MPa and Poisson ratio 0.34 . The equivalent stiffness K_{tube} of the measuring tube, obtained as described in Section 3.3, is found to be 483.5 N/mm. The simulations of the Coriolis flowmeter operation were performed for a water-like fluid ($\rho_F = 1000\,\text{kg/m}^3$ and $\mu = 1 \times 10^{-3}\,\text{Pa s}$) and for four different fluid average axial velocities v_{F}: 0.1, 0.4, 2.0 and 5.0 m/s.

The FE and FV domain discretization applied to the structural domain and the fluid, respectively, is schematically shown in Fig. 9. It consists of 4000 shell type FEs and 67 392 FV cells, where 41 600 FV cells pertain to the measuring tube domain. In the longitudinal direction, a fine equidistant mesh is applied to that part of the fluid–structure domain that vibrates. The remaining part, i.e. the inlet and outlet subdomains, are discretized non-equidistantly with a monotonic coarsening of the mesh in the direction of the ends of the modelled domain. In order to capture the fluid viscosity effects close to the tube inner surface properly, a density of the FV mesh is adequately increased in the radial direction.

For all coupled simulations performed, a single oscillation cycle was divided into 140 equal time steps. For displacement and velocity integration, the Newmark formula was used with parameters α_β and α_γ set to $\frac{4}{9}$ and $\frac{5}{6}$. Such values are recommended as they provide artificial damping of high frequency vibrations at the beginning of the coupled simulation.

The evaluation of the first damped frequency ω_D and the damping factor ζ of the fluid-conveying measuring tube in free vibration were completed after the quantities of interest were within the prescribed tolerance interval $\varepsilon_D = 0.001$, where as the inner iteration loop in a single time step was finished when the norm (16) became smaller than prescribed tolerance $\varepsilon_P = 0.002$.

The simulations were run on a PC with a 3 GHz AMD Athlon processor and with 2 Gbyte RAM, operating under Windows XP OS. Each simulation required about 3 days of wall clock time, when, after introducing the driven motion, approximately 15 oscillation periods were completed.

4.1. Analysis of free vibration response

Computational efficiency of the numerical strategies, proposed in Section 3.2, has been tested for fluid flow through the Coriolis flowmeter at an average axial velocity of 5 m/s. First, let us observe the free oscillation response

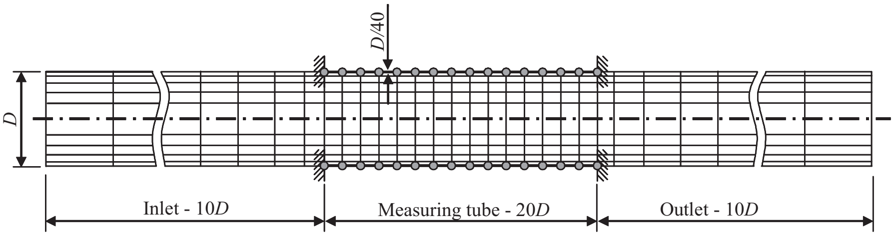

Fig. 9. Schematic representation of the computational domain discretization.

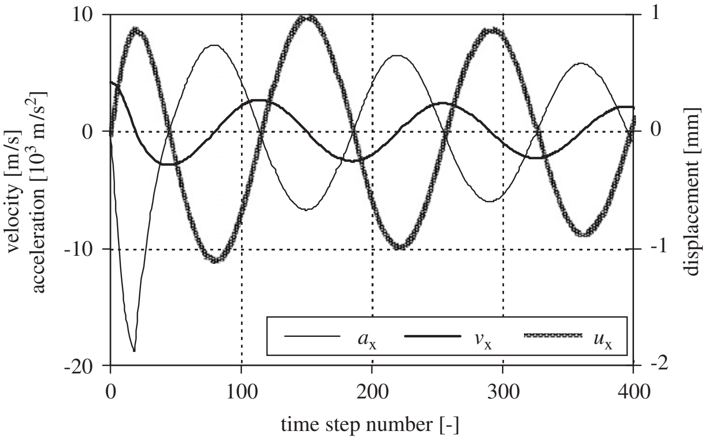

Fig. 10. Time variation of kinematic values at point M (Scenario 3).

(displacement u_x, velocity v_x and acceleration a_x) of the measuring tube in Fig. 10, which is practically the same, regardless of the fluid load application scenario applied (scenarios are defined in later in this section). The damping factor obtained with the simulation is equal to 0.016, which is significantly higher than that of the empty tube, which was set to 0.001. The minor part of such increase is caused by the actual fluid damping, whereas its major part is due to numerical causes. Relatively high damping is caused by the selected time step size [see Bobovnik et al. (2005)] and by the combination of flow and solid time integrator solvers (Euler implicit and Newmark, respectively), which introduce the non-physical time lag between the solutions of the respective time domains [see Piperno and Farhat (2001) for loosely coupled algorithms]. The application of the second-order Crank–Nicholson scheme for the fluid subdomain, which further reduced the damping of the coupled system by about 40%, clearly shows that the origin of augmented damping is indeed in the numerics. However, a comparison of results obtained for both fluid time schemes showed that the phase difference calculated using Euler implicit scheme exhibited much greater stability, which was one of the primary concerns in our analysis. The results of simulations that follow are therefore all obtained using Euler implicit scheme.

Next, the three different fluid load application scenarios were considered:

(i) Scenario 1: The fluid load computed in the initial time step is applied to the tube in its total amount in the subsequent time step.
(ii) Scenario 2: The actual fluid load is considered in the analysis of the dynamic response of the tube only after the initial time delay. It has been found convenient to associate this time delay with the time needed for the measuring tube to reach its maximum deflection (i.e. zero velocity position) for its first time in the initial stage of the simulation.
(iii) Scenario 3: In contrast to Scenario 2, the fluid load is applied in a smooth way after the same time delay.

The time variations of the load factor $\alpha(t)$ (Fig. 7) were defined in the analysed cases with the following combinations of parameters n_1 and n_2: $n_1 = 0$, $n_2 = 1$ (Scenario 1), $n_1 = 20$, $n_2 = 21$ (Scenario 2) and $n_1 = 20$, $n_2 = 45$ (Scenario 3). In contrast to Scenarios 1 and 2, which employ the zero-order fluid stress tensor predictor, the three-point predictor was introduced in Scenario 3.

In the analysis of the fluid–structure response obtained in the investigated coupled simulations, attention has to be paid to the proper selection of quantities to be considered in such an analysis. Observing only the motion exhibited by point M in the central cross-section of the tube (Fig. 6) would probably lead to a wrong conclusion. Namely, the response of the measuring tube displayed in Fig. 10, suggests that initial disturbance, caused by pushing the tube into motion, disappears in one single oscillation cycle. In contrast to the behaviour exhibited by point M, the difference between the responses of the sensing points S_1 and S_2 (that are also used for the calculation of the measuring effect) proves to have a longer transient regime, which is shown in Fig. 11 for Scenario 3.

The same quantities as in Fig. 11 are also presented in Fig. 12 for the three scenarios considered. Scenario 1, which can be treated from the point of application of the fluid load as a "sharp" one, performs very badly, as seen from the graphs. By including the computed fluid load, which results from oscillation of the tube at the very beginning of the simulation, a relatively large initial disturbance (because the measuring tube is pushed into motion from rest) is introduced into the simulation, so that the rate of convergence is seriously damaged. In that case, the stabilized response at the sensor locations was obtained only after 20 oscillation cycles. Great improvement in stabilization of the analysed response was demonstrated by Scenario 2 with the delayed fluid load application. Namely, only eight oscillation cycles were needed to obtain the stabilized solution.

However, with the zero-order fluid stress tensor predictor, about nine iterations per time step were needed in average. To reduce this rather large number of inner iterations per time step, the three-point fluid stress tensor predictor that is based on the known fluid stress data from the preceding three time steps has been introduced. Starting the inner iteration loop in the actual time step by the so-defined fluid load estimation, practically halved the number of inner iterations per time step. The impact of introducing the described three-point predictor instead of the one-point predictor on the computation efficiency is more than evident from the histogram in Fig. 13. Using Scenario 3, the stabilized response at the sensor locations was achieved after only six oscillation cycles.

Despite the fact that the time delay and the smooth application of the fluid load in the beginning of the simulation obstruct the model from reflecting the actual physical initial conditions and thereby do not make it possible to observe the actual transient response, such a scenario was proved to be very efficient and robust for our purposes where the steady state response is sought. Its application also abolishes all preceding operations or simulations, which would be needed to assure the proper (real) initial conditions for the considered fluid-measuring tube system.

4.2. Transition from free to forced vibration

The numerical model, taking Scenario 3 into account, was tested for fluid flow through the straight measuring tube of the Coriolis flowmeter for four different average axial flow velocities. With the intention that the numerical model would resemble the true operation of the flowmeter as much as possible, the exciting force is included in the model to obtain the forced response of the measuring tube, as described in Section 3.3.

To obtain the magnitude of the respective exciting force, first the damped natural frequency ω_D and the damping factor ζ have to be determined. As seen from the tabulated results in Table 1 the damped natural frequency decreases slowly with the decreasing of axial velocity of the fluid, as expected according to Kutin et al. (2006). On the other hand, the damping factor remains constant. It is determined mainly by the used coupling procedure rather than by the true mechanical properties of the dynamic system. Table 1 also shows that although rather different axial fluid velocities were considered, the displacement amplitude u_0 and consequently the excitation force amplitude F_0 remain constant, meaning that the forced vibration began at approximately the same time for all the simulated cases.

When considering the established computational performance in Step II, we are first interested in the stabilized fluid–structure response and smooth transition from free to forced vibration. It is more than evident that the applied harmonic excitation at point P, with its parameters being determined by the approach described above, contributes significantly to fast convergence. Observation of the motion exhibited by point M, which is displayed graphically in Fig. 14, shows that, after the excitation force is entered in the computation, the amplitudes of the kinematic values remain almost unchanged. It is also evident that transition from free to forced vibration remains undisturbed (even in terms of the number of inner iterations), when proper amplitude and phase lag of the excitation force are determined and included in the computational model.

A valuable quantity for characterizing the quality of the imposed excitation is the phase difference $\Delta\phi_M$ established between the displacement of point M and the excitation force. It is found that for all considered cases the phase difference differs about 2.5° from the ideal value of 90° at resonance. The time evolution of the observed phase difference for the analysed case with average axial velocity of 5.0 m/s is presented in Fig. 15. The applied excitation frequency deviates from the true natural frequency of the measuring tube by approximately $\varepsilon_\omega = \zeta|\frac{\pi}{2} - \Delta\phi_M|100\%$, where $\Delta\phi_M$ is expressed in radians. Thus, the excitation frequency ω_0 deviates systematically for only 0.07% from the

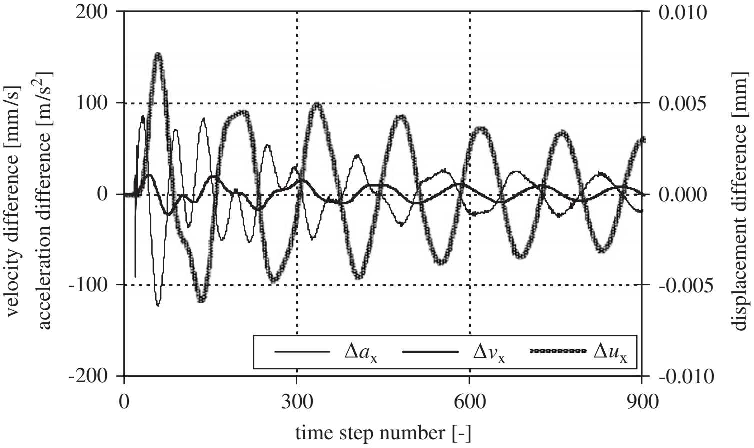

Fig. 11. Time variation of difference between kinematic values at sensing points S_1 and S_2 (Scenario 3).

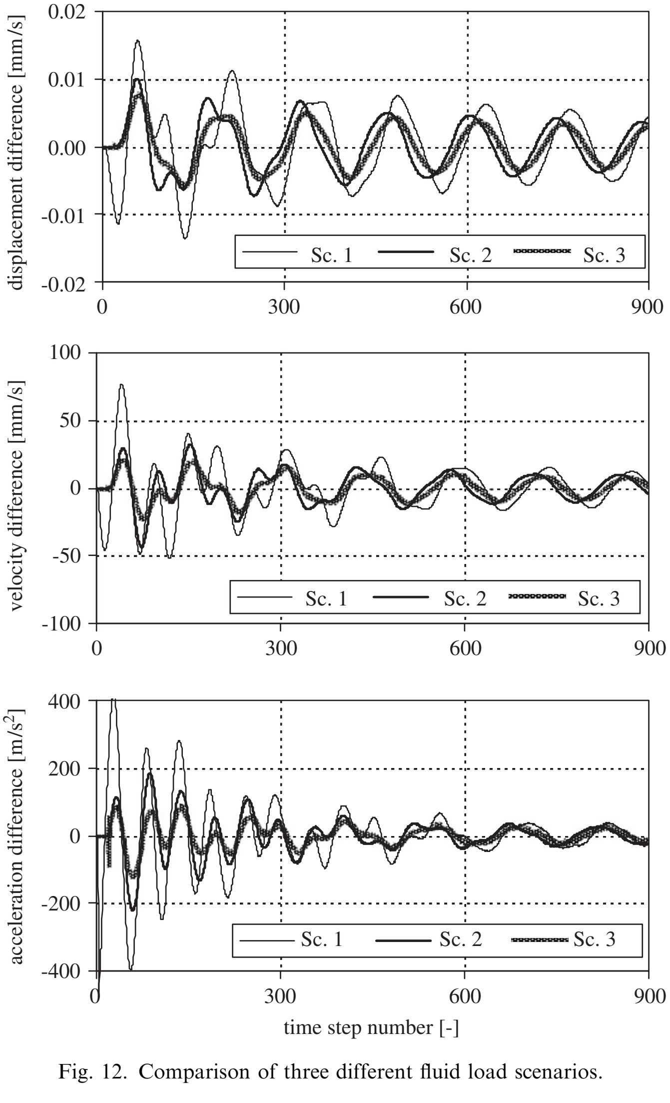

Fig. 12. Comparison of three different fluid load scenarios.

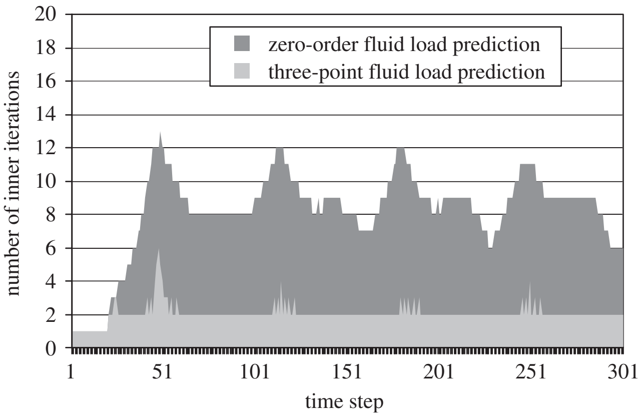

Fig. 13. Influence of the fluid load predictor on the number of inner iterations.

Table 1

v_{inflow} (m/s)	Step I: numerical results			Step II: computed values	
	ω_D (1/s)	ζ (–)	u_0 (mm)	ω_0 (1/s)	F_0 (N)
5.0	2617.67	0.0159	0.86	2618.00	13.3
2.0	2617.67	0.0159	0.86	2618.00	13.3
0.4	2617.65	0.0159	0.86	2617.98	13.3
0.1	2617.31	0.0159	0.86	2617.64	13.3

true natural frequency of the measuring tube. Kutin and Bajsić (2002) have found that the same order of deviation may be expected for the phase difference between the computed responses at the sensor locations, and even 10 times lower deviation for the corresponding time difference. The latter is favourable from our point of view because, as shown in the next section, it is the time difference which defines the measuring effect of the Coriolis flowmeter.

4.3. Measuring characteristics

The Coriolis measuring effect is represented by the phase or time difference between the motion of sensing points S_1 and S_2 exhibited due to the mass flow rate through the measuring tube. The phase difference is obtained from the steady-state resonant responses of points S_1 and S_2 in Step II. The phase of each individual response observed for a window width of 10 oscillation periods is obtained using a DFT (discrete Fourier transform) algorithm, and the phase difference is calculated as the difference between the phase values of the two responses. The result obtained from the last 10 periods is further used as the calculated phase difference. Fig. 16 represents phase differences for four different axial flow velocities in the measuring tube. One can see that the observed phase differences encountered in the considered straight tube Coriolis flowmeters are of order of magnitude lower than one degree, and that the predicted measuring characteristic (variation of the phase difference with the average fluid velocity) of the flowmeter is approximately linear.

A more detailed insight into possible nonlinearities in the measuring characteristics can be given by the mass flow rate sensitivity. It is defined by the ratio between the time difference ($\Delta t_S = \Delta\phi\ /\omega_0$) exhibited by the respective responses at two measuring points S_1 and S_2 and the mass flow rate q_m through the measuring tube, $K_{\Delta t} = \Delta t_S/q_m$.

The thus defined sensitivity may be affected, as already shown in some of our previous work (Kutin et al., 2006), by the axial flow velocity, or better said with the Reynolds number in the measuring tube. For a better comparison with previously published results, the mass flow rate sensitivity obtained with the current numerical model is presented in terms of dependence on Reynolds number. Fig. 17 shows its relative variation with respect to the value obtained for the highest Reynolds number simulated. Let us state, for better visualization of the magnitude of the measuring effect, that the sensitivity for $\mathrm{Re} = 10^5$ is equal to $2.885 \times 10^{-6}\ \mathrm{s^2/kg}$. The maximum nonlinearity in the observed range of Reynolds

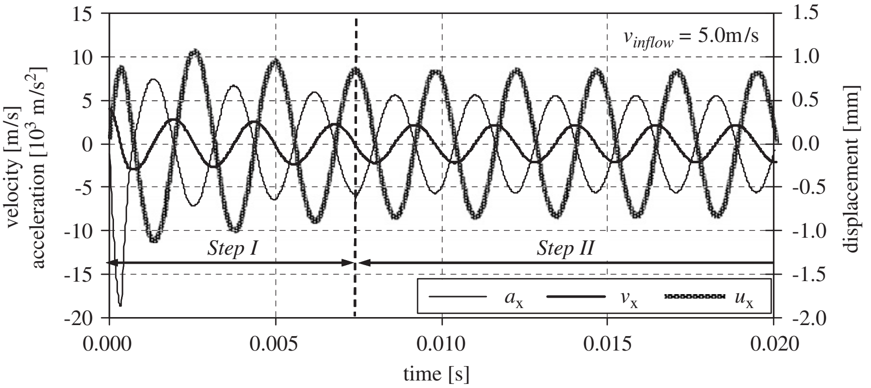

Fig. 14. Time variation of kinematic values at point M.

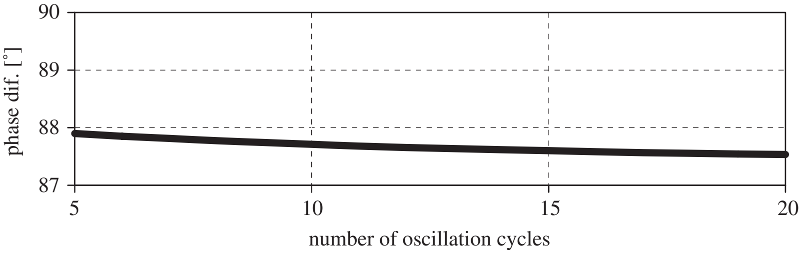

Fig. 15. Time variation of the phase difference $\Delta\phi_M$.

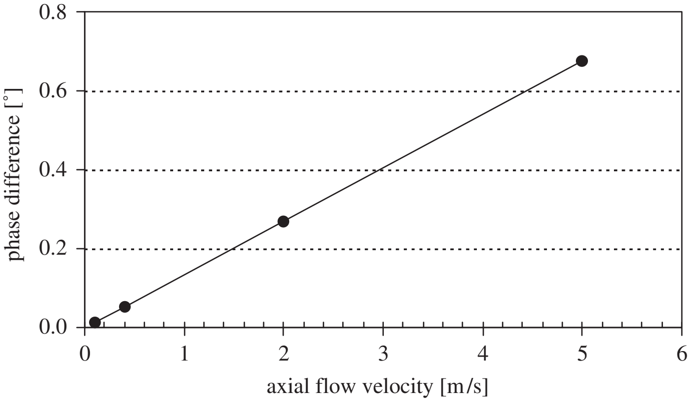

Fig. 16. Phase difference between the sensing points S_1 and S_2 for four different fluid average axial velocities.

numbers is about 0.4%. This result is in reasonable agreement with existing findings of the analytical weight vector theory (Kutin et al., 2006), which predicts a decrease of sensitivity of about 0.3% for the same flowmeter configuration.

When evaluating the measuring effect, especially for low mass flow rates, we have to be aware of the effect of relative increase of noise (physical and numerical) present in the flowmeter. The magnitude of this effect presented in Fig. 18 is estimated as the standard deviation of the calculated mass flow sensitivities (phase differences) over the last 14 periods (with moving-window width of 10 periods). As seen, higher scattering (standard deviation) of results is predicted for lower Reynolds numbers, which resembles the phenomena experienced in commercial flowmeters (zero stability). In view of the relative standard deviations being significantly below 0.1%, we can claim that we have accomplished one of our main objectives, which was to build a numerical model resembling the true operational conditions of the Coriolis flowmeter, with capability of catching sensitivity variations of order of magnitude around tenths of a percent.

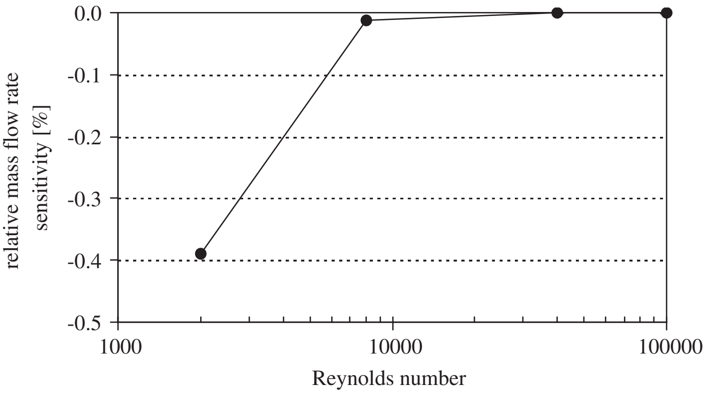

Fig. 17. Variation of the relative mass flow rate sensitivity with Reynolds number.

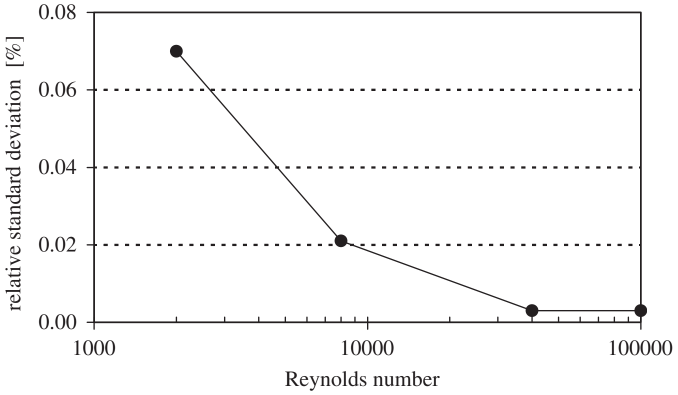

Fig. 18. Variation of the relative standard deviation of the mass flow rate sensitivity with Reynolds number.

5. Conclusions

The numerical model of a Coriolis flowmeter, where the primary sensing element is a straight-tube vibrating under imposed forced vibration conditions, is presented in the paper. In the considered coupled fluid–structure problem, which is solved by adopting a partitioned analysis approach, the FVM and FEM are used, respectively, for a discrete solution of the fluid and structural dynamics problem. The respective coupled computation is performed by following a staggered solution procedure including the inner iterations to assure strong coupling of the computational domains. In order to minimize the computational time needed to obtain the stabilized response of the measuring tube, we tested three different scenarios. It was established that the three-point prediction of the fluid load and its gradual application to the structure, which is realized over several time steps in the initial stage of the simulation, is computationally efficient, thus significantly shortening the transient response of the periodically oscillating system. In addition to that, a harmonic excitation force was also included in the numerical model, an action which additionally reduced the computational time and contributed to continuous constant magnitude response.

The presented model, whose behaviour exhibits a good resemblance with the actual operation of Coriolis flowmeters, was further applied to study the nonlinearity of the Coriolis flowmeter, exhibited at lower mass flow rates. The mass flow rate sensitivity of the straight-tube beam-type flowmeter was obtained from the time difference between the motions of the sensing points positioned symmetrically to the tube length. The decrease of sensitivity, of about 0.4% was predicted for transition from turbulent to laminar flow. It was shown that this result reasonably agrees with previous findings about the magnitude of the velocity profile effect (Kutin et al., 2006). Besides, it was clearly manifested that the scatter of the computed mass flow sensitivities is small enough to allow the use of the presented model for investigation of such small sensitivity variations.

The numerical model presented herein has the capability of being further employed for investigation of different flowmeter designs and their susceptibility to different effects, particularly those related to the fluid flow, such as the already presented velocity profile effects, the installation effects, operation of flowmeter with highly viscous fluids or compressible fluids.

References

Baker, R.C., 2000. Flow Measurement Handbook: Industrial Designs, Operating Principles, Performance, and Applications. Cambridge University Press, Cambridge.

Bobovnik, G., Mole, N., Kutin, J., Štok, B., Bajsić, I., 2005. Coupled finite-volume/finite-element modelling of the straight-tube Coriolis flowmeter. Journal of Fluids and Structures 20, 785–800.

Engel, M., Griebel, M., 2006. Flow simulation on moving boundary-fitted grids and application to fluid–structure interaction problems. International Journal of Numerical Methods in Fluids 50, 437–468.

Farhat, C., Lesoinne, M., 2000. Two efficient staggered algorithms for the serial and parallel solution of the three-dimensional nonlinear aeroelastic problems. Computer Methods in Applied Mechanics and Engineering 182, 499–515.

Felippa, C.A., Park, K.C., Farhat, C., 2001. Partitioned analysis of coupled mechanical systems. Computer Methods in Applied Mechanics and Engineering 190, 3247–3270.

Ferziger, J.H., Perić, M., 1999. Computational Methods for Fluid Dynamics, second ed. Springer, Berlin.

Kutin, J., Bajsić, I., 2002. An analytical estimation of the Coriolis meter's characteristics based on modal superposition. Flow Measurement and Instrumentation 12, 345–351.

Kutin, J., Hemp, J., Bobovnik, G., Bajsić, I., 2006. Velocity profile effects in Coriolis mass flowmeters: recent findings and open questions. Flow Measurement and Instrumentation 17, 349–358.

Matthies, H.G., Steindorf, J., 2003. Partitioned strong coupling algorithms for fluid–structure interaction. Computer and Structures 81, 805–812.

Matthies, H.G., Niekamp, R., Steindorf, J., 2006. Algorithms for strong coupling procedures. Computer Methods in Applied Mechanics and Engineering 195, 2028–2049.

Païdoussis, M.P., 1998. Fluid–Structure Interactions: Slender Structures and Axial Flow, vol. 1. Academic Press, London.

Païdoussis, M.P., 2004. Fluid–Structure Interactions: Slender Structures and Axial Flow, vol. 2. Elsevier Academic Press, London.

Piperno, S., 1997. Explicit/implicit fluid/structure staggered procedures with a structural predictor and fluid subcycling for 2D inviscid aeroelastic simulations. International Journal for Numerical Methods in Fluids 25, 1207–1226.

Piperno, S., Farhat, C., Larrouturou, B., 1997. Partitioned procedures for the transient solution of coupled aeroelastic problems—part I: model problem, theory and two-dimensional application. Computer Methods in Applied Mechanics and Engineering 124, 79–112.

Piperno, S., Farhat, C., 2001. Partitioned procedures for the transient solution of coupled aeroelastic problems—part II: energy transfer analysis and three-dimensional applications. Computer Methods in Applied Mechanics and Engineering 190, 3147–3170.

Pope, S.P., 2000. Turbulent Flows. Cambridge University Press, Cambridge.

Thomas, P.D., Lombard, C.K., 1979. Geometric conservation law and its application to flow computations on moving grids. AIAA Journal 17, 1030–1037.